Supplementary Information

Crystal growth of calcium oxalate mono- and dihydrate under laminar flow in microfluidic devices

1.The overview of mold and chip

The transparent Polydimethylsiloxane (PDMS) mixture is put onto the silicon wafer (see Figure 1.a) produced microfluidic device (see Figure 1.b) by lithography technique in the clean room.

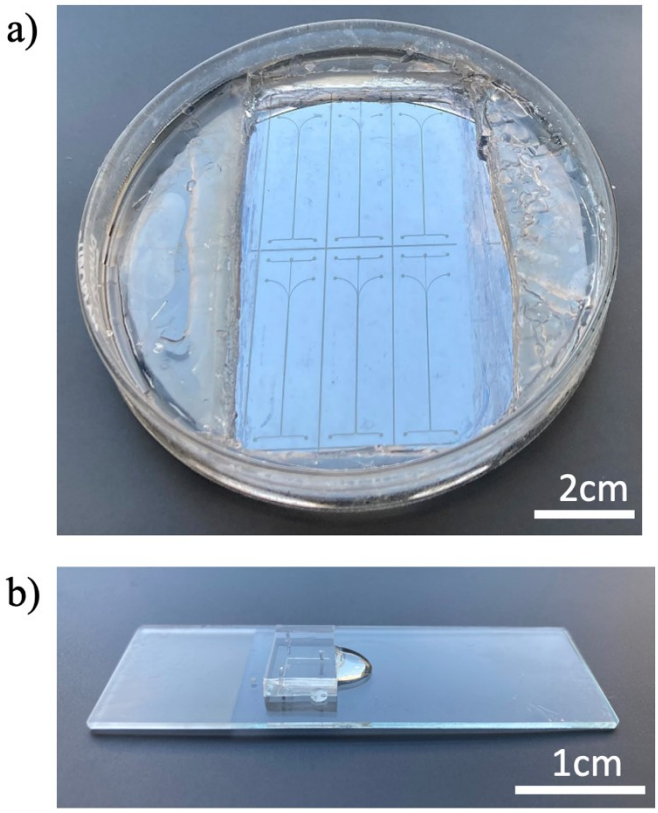

Figure S1. a) Silicon wafer to use in the production of PDMS chip. b) A closed microfluidic chip placed on PDMS coated glass slide after spin coating.

2. COMSOL Model

Velocity profiles in the channel were used in COMSOL to model concentration profiles and crystal growth. The reaction term was not included in the COMSOL model due to the reaction's limited growth kinetics. We have calculated Damköhler number (Da) as $8.11 \cdot 10^{-6}$. If Da is smaller than 1, the reaction between species is very slow compared to the diffusive mass transport of the species towards the surface.[1]

Because the Reynold number Re < 2000 (Re=6.7 at the maximum velocity of 0.075 m/s) and because the species were sparsely dissolved, a laminar flow and transport of two diluted species was chosen for the 3D analysis. Polygons and arcs were chosen in COMSOL as sketch functions to draw the geometry of the channel. While the height and width of the channel had the same size, the length of inlets is decreased from 1500 µm to 1400 µm, and the length of the main channel was reduced from 6000 to 1500 µm. In this way, the created mesh had fewer elements and it took less time to compute without dramatically affecting the results (Figure 2). Automatically generated COMSOL microchannel mesh includes 317,354 domain, 38,130 boundary and 1,649 edge elements (in Figure 2.b).

Once the mesh was fixed, laminar flow conditions were applied. Fully developed flows with the chosen average velocity were used for the two inlets and the outlet was set as a constant pressure boundary at 101,325 Pa.

Next, the transport equations for diluted species were solved with diffusion coefficients $0.793 \cdot 10^{-10}$ m^2/s for calcium and $0.987 \cdot 10^{-10}$ m^2/s for oxalate.[2, 3] Only Ox^{2-} was introduced in the upper inlet and only Ca^{2+} was introduced in the lower inlet at the channel.

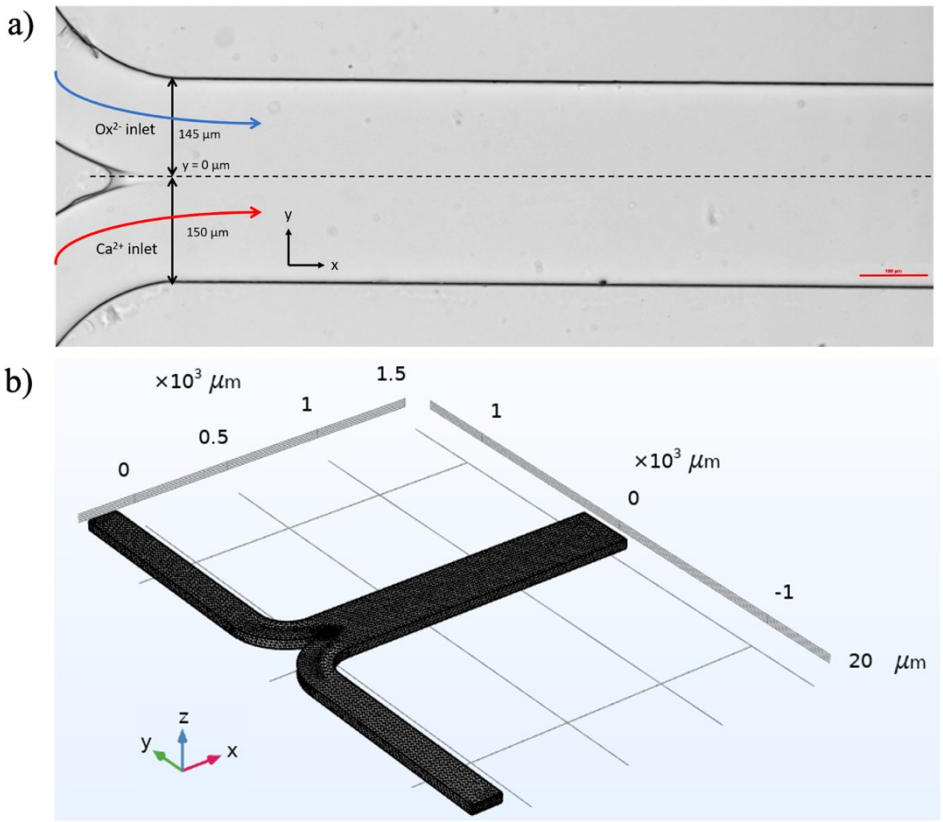

Figure S2.a) The view of the channel of microfluidic device. b) Automatically generated COMSOL microchannel mesh includes 317,354 domain, 38,130 boundary and 1,649 edge elements.

3. COMSOL Velocity Profiles in the Microchannel

The COMSOL model calculated velocity profiles are shown in several slices throughout the main channel for U = 0.075 m/s in Figure 3.a. The v-profile at x = 800 µm is shown in Figure 3.b as a single slice (sample AU3 in Figure 4 in the manuscript). Due to the height value (45 µm) being 6.6 times less than the width 295 µm, the majority of the xy-plane is equivalent to a situation with two "infinite" parallel plates, resulting in a parabolic Poiseuille-flow in the xz-plane (Figure 3.c). The v-profile is plug-flow-like in the xy-plane, which is due to very small height compared to width[4]. The no-slip condition causes the velocity to decrease towards the walls. As a result, except at its edges, the v in the xy-plane is uniform (Figure 3.d). When varying oxalate inlet concentrations and/or average velocities, similar v-profiles are seen, where the maximum velocity in the channel (U_{max}) corresponds to U as U_{max} = 3/2 U. Besides this, velocity conditions at the bottom and the top of the channel are equal because of the negligible gravity in the Navier-Stokes equations.

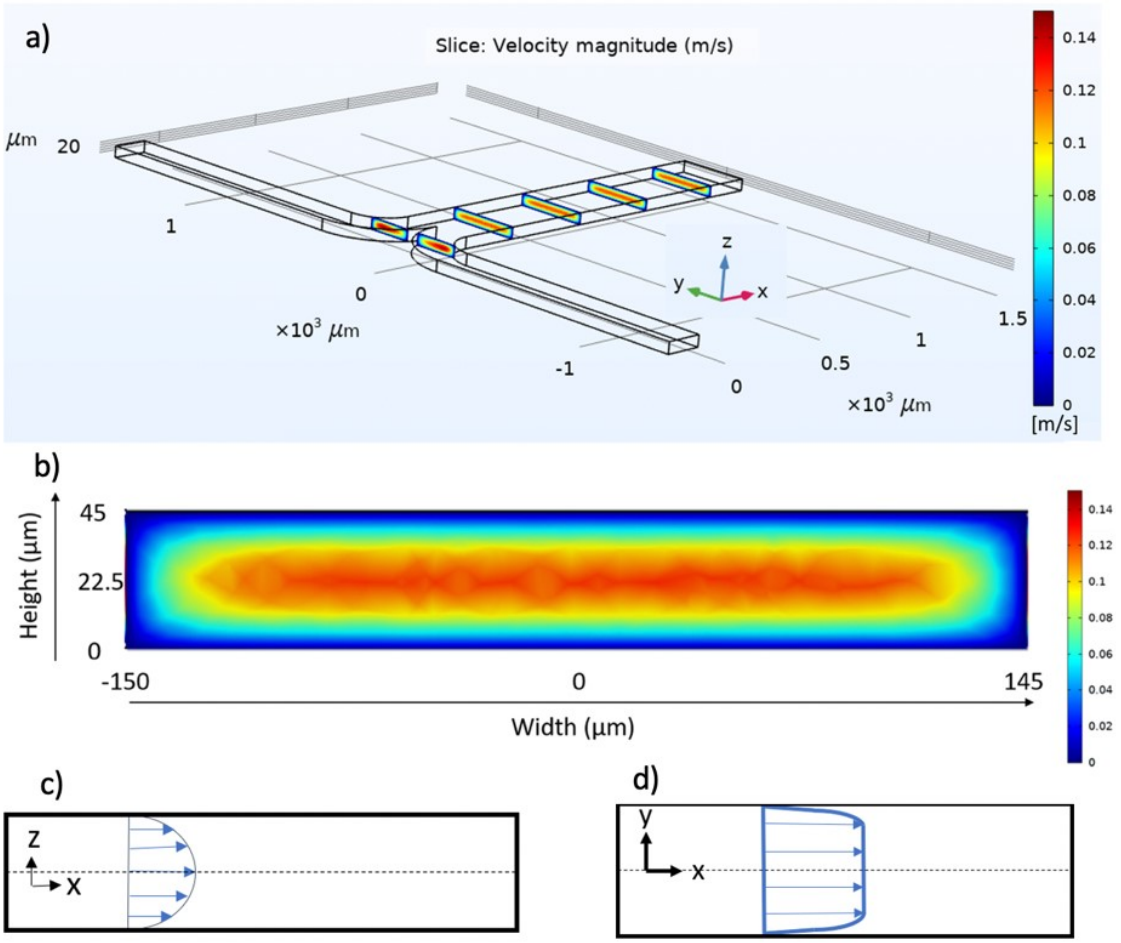

Figure S3.a) 3D v-profiles through the main channel of the microfluidic device at different fixed length positions for sample AU3 in Figure 4 in the manuscript. (b) One example of 3D plot of the v-profile as a single slice at x = 800 µm(AU3 in Figure 4). (c) Sketch of the parabolic v-profile in the xz-plane. (d) Sketch of the plug flow behavior of the v-profile in the xy-plane (AU3 in Figure 4).

The effect of varying U is studied by simulating the three velocities in ultrapure water conditions, such that $c_{ca,o}$ = 12 mol/m^{3}and $c_{ox,o}$ = 1.6 mol/m^3, after which these results are analyzed to deduct σ-profiles and areas. In the Ox^{2-}-rich side at the channel bottom, COM and COD boundaries, as well as the maxima, are barely affected by U, since their graphs greatly overlap (Figure S4). The same trend occurs in the Ca^{2+}- rich side.

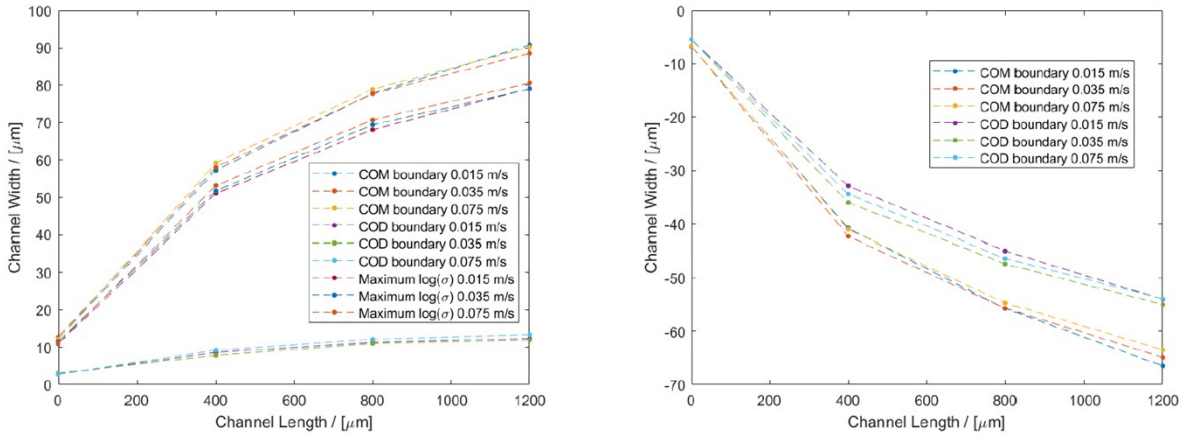

Figure S4: σ-boundary and maxima for the channel width vs length at three different velocities u = 0.015/ 0.035/ 0.075 m/s (a) σ-regions at the channel bottom (z = 0µm) for COM and COD in the Ox^{2-}-rich part of the channel. The upper three graphs are the upper COM boundaries, the middle three graphs the upper COD boundaries, and the lower three graphs are at maximum σ.(b) σ-regions at the channel bottom (z = 0µm) for COM and COD in the Ca^{2+}-rich part of the channel. The upper three graphs are the lower COD boundaries and the lower three graphs are the lower COM boundaries.

4. Finding supersaturation (σ) values using Jess

The initial concentration of compounds and temperature value were added to find the supersaturation values using Jess for different experiment conditions. The overview of the program is below. Jess Urine Expert program is applied to calculate supersaturation of artificial urine to estimate σ-profiles in the channel. Due to OPN and creatinine are not in Jess, we are not considering OPN to find σ-profiles.

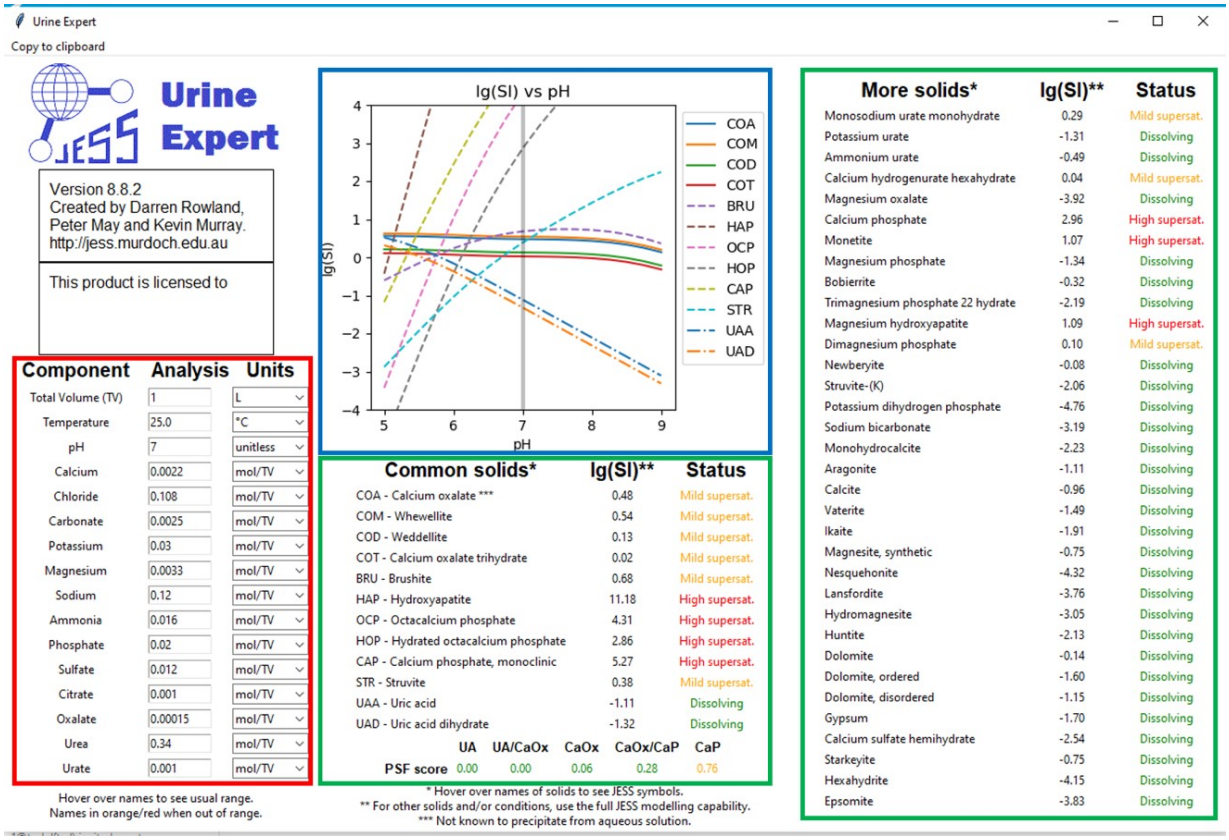

Figure S5. Overview of Jess program. Red rectangular shows the workspace to add initial compositions. In the blue and green colors where are the outputs composition from program workspace.

5. The calculation method of Crystal Growth Rate

The image analysis tool Cellprofiler was used to analyze crystal images from experiments. From the images of channels to single crystal, the “Imagemath » Invert » Crop” module is used. Following the “IdentifyPrimaryObjects” module is to identify the crystal with a built-in thresholding system and “MeasureImageAreaOccupied”.

6. Evaluation supersaturated area with applying COMSOL and JESS

The estimated concentration values of calcium and oxalate from COMSOL were used in JESS to find supersaturation values of COM and COD in the channel. With this way from lowest to highest supersaturation values area (Figure 5) were found and it was seen that crystals emerged between this area (Figure 3 in manuscript).

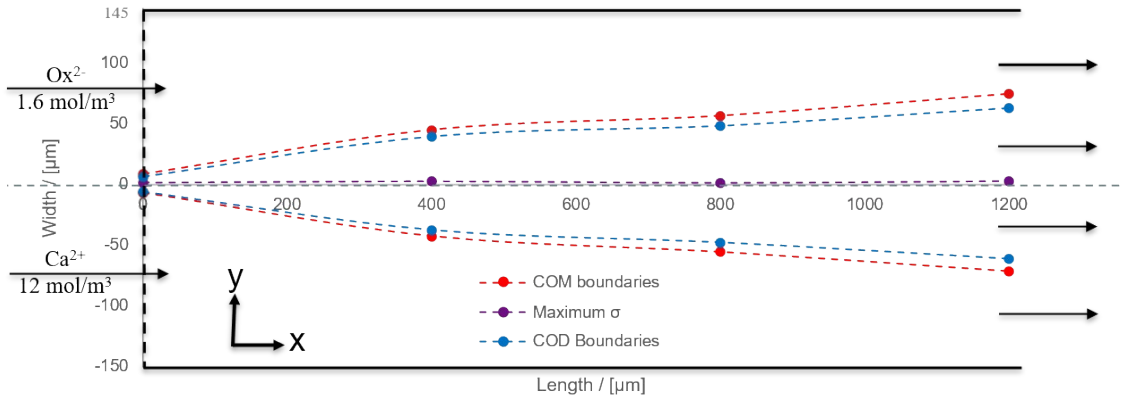

Figure S6. 2D display of σ boundaries of COM (red dots) and COD (blue dots) at the channel bottom (z = 0 µm) in artificial urine with [Ca]=12 mmol/m³ and [Ox]=1.6 mmol/m³ at U=0.035 m/s as sample AU2 (see Figure 3&4 in the manuscript). Highest σ is seen with purple color, it is log (σ)= 1.67 for COM and log (σ)= 1.25 for COD.

7. Identification of crystals via Raman spectroscopy

After completing the experiments, the crystals in the microchannels were identified using Raman Spectroscopy (Horiba Scientific Raman Spectroscope, Japan) without removing crystals from the channels. The peaks in the Raman spectrum were determined with a script which is written in Matlab in Chemical Engineering.[5] The observed peak shifts from channels were compared with literature values in Table 1. The Raman measurement for different samples is shown in Figure 8 in which Raman shifts associated with COM are indicated in red, COD in green, PDMS in purple, and urea in black colour circles. Calcium oxalate monohydrate ($CaC_2O_4 \cdot H_2O$, Sigma-Aldrich, CAS563-72-4, St. Louis, MO, USA) was mixed with artificial urine and sent to the chip (Figure 8.a). The suspensions were left undisturbed for overnight to allow the crystals to sediment. The crystals were then placed on a glass slide for analysis. The Raman spectrum has COM peaks at 896, 1463, and 1490 cm^{-1} in Figure 8.a. Another peak value at 1004 cm^{-1} is seen which represents urea present in artificial urine.[6] Only PDMS is used to find the spectrum in Figure 8.b. It shows Raman shifts similar to literature values for PDMS, with peaks at 490, 616, 709, 1262, and 1411 cm^{-1}. The slight difference in peaks compared to literatures values could be due to the ratio of the mixture of PDMS and the curing agent which is used to fabricate PDMS chip in Table 1.[7] The spectrum from the tetragonal crystal image in sample AU1 (in Figure 4 in the manuscript) gave peaks at 910 and 1477 cm^{-1} for COD (green) and the peaks from PDMS (purple) see Figure 8.c. A second tetragonal crystal image from sample AU7 (Figure 6 in the manuscript) showed peaks at 1474-1478, representing COD (green) among PDMS peaks (purple) see Figure 8.d.

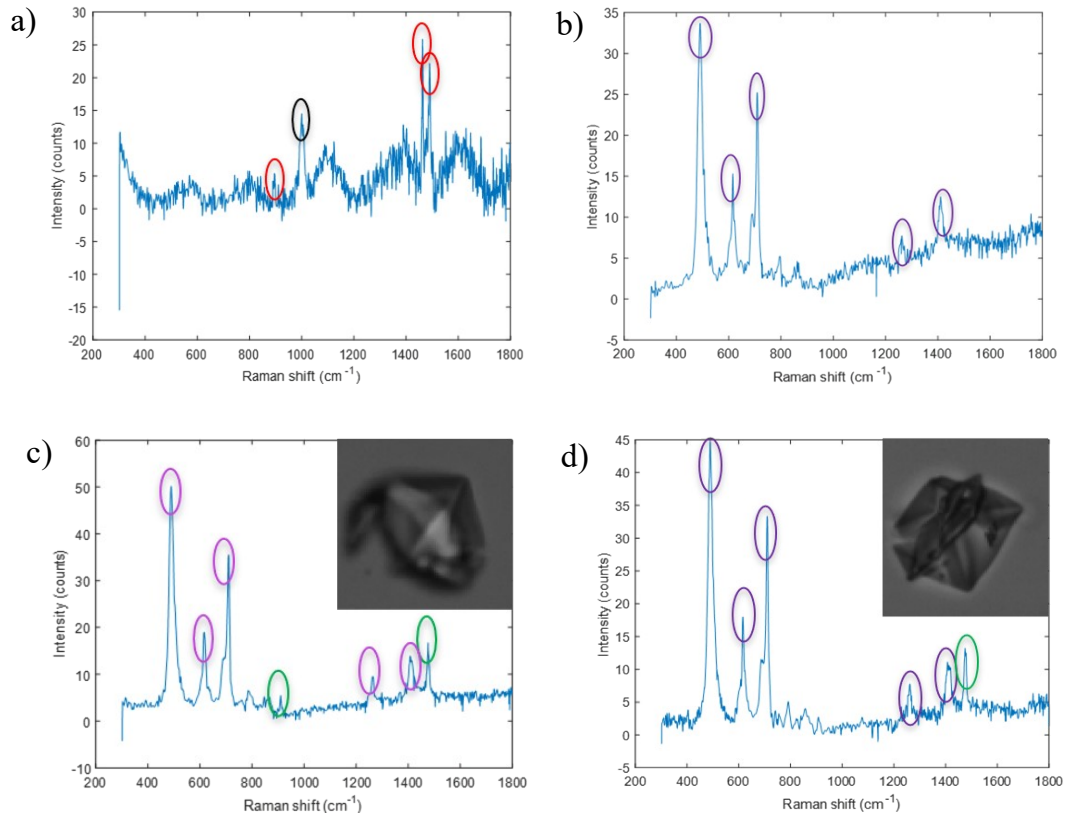

Figure S7. The results of Raman spectroscopy to identify COM and COD crystals in the microfluidic device. Peaks encircled in black, red, green and purple are associated with urea, COM, COD and PDMS, respectively. (a) COM powder mixed with artificial urine and placed on glass slide, (b) PDMS material is used to identify background peaks from crystals. (c) Raman peaks from COD crystal from sample AU1(Figure 4 in the manuscript) at the right top corner. (d) Raman peaks from second COD crystal from sample AU7 (Figure 6 in the manuscript at the right top corner).

Table 1. Raman shift peak values for COM, COD, and PDMS.

COM shifts [cm^{-1}][8 9 10 11]	**COD shifts [cm^{-1}]**[8 9 10 11]	**PDMS shifts [cm^{-1}]**[12 13]
503, 504, 506	507, 508	488, 492,
896, 897	910, 912	618.5
1463	1474, 1477, 1478	688
1487, 1488, 1489, 1490, 1492	1632	707, 710, 712
1630, 1631	-	1265, 1414

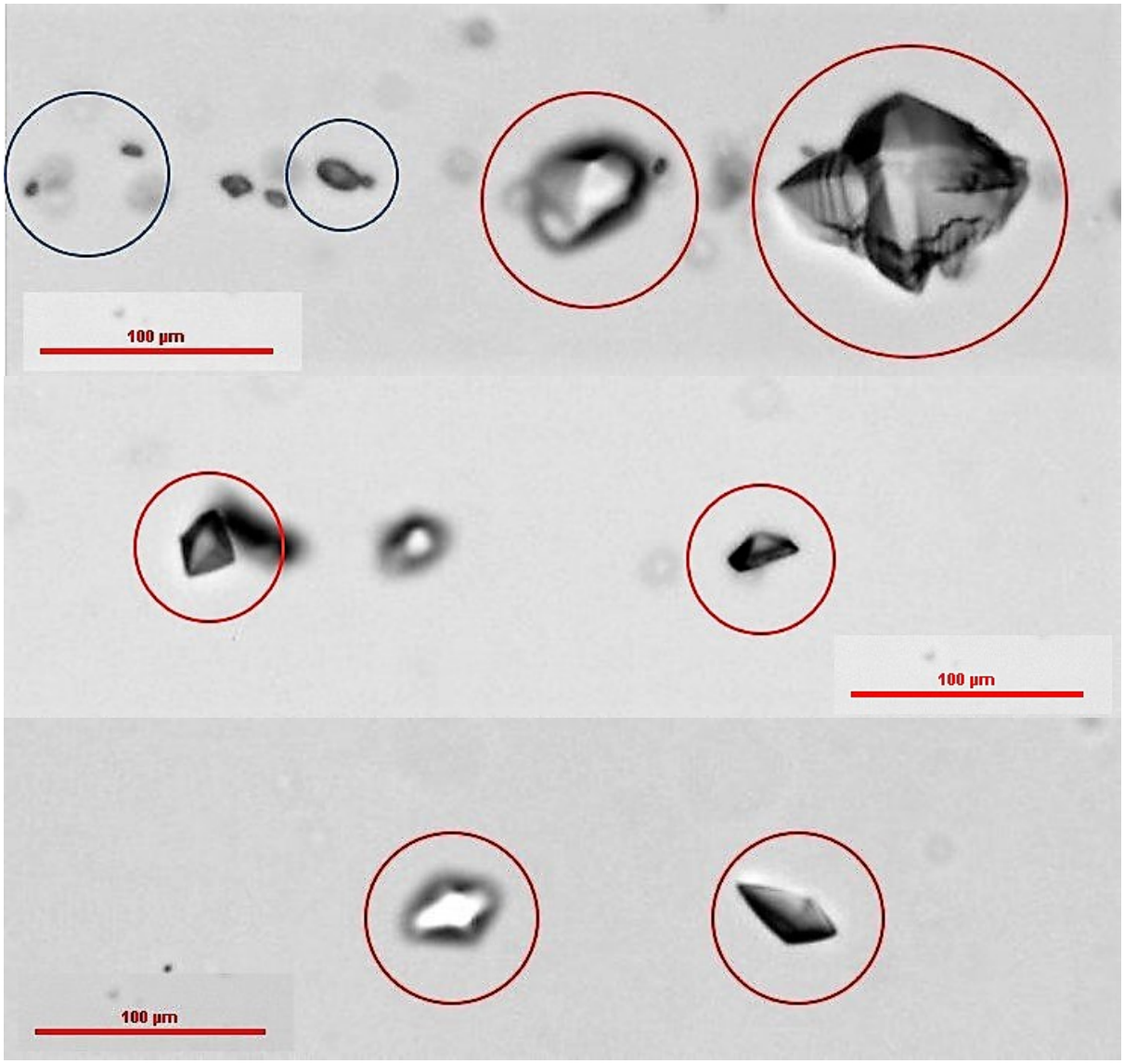

Figure S8: Zoomed-in images of COM and COD crystals at t = 7.3 min in conditions AU4, circled blue and red, respectively.

8. References

1. Kassemi, M.; Brock, R.; Nemeth, N., A combined transport-kinetics model for the growth of renal calculi. *Journal of Crystal Growth* **2011,** *332* (1), 48-57.
2. Nielsen, A., Transport control in crystal growth from solution. *Croatica Chemica Acta* **1980,** *53* (2), 255-279.
3. Nielsen, A. E., Theory of electrolyte crystal growth. The parabolic rate law. *Pure and Applied Chemistry* **1981,** *53* (11), 2025-2039.
4. Thompson, B. W., Secondary flow in a Hele-Shaw cell. *Journal of Fluid Mechanics* **1968,** *31* (2), 379-395.
5. Matlab Peak raman spectroscopy. http://matlab.cheme.cmu.edu/2012/08/27/peak-finding-in-raman-spectroscopy (accessed March 2021).

6. de Souza V, E. E., Bispo, J.A.M., Silveira, L.J., Fernandes, A.B., Discrimination model applied to urinalysis of patients with diabetes and hypertension aiming at diagnosis of chronic kidney disease by Raman spectroscopy. *Lasers in medical science* **2017,** *32* (7), 1605-1613.
7. Cruz-Felix, A. S.; Santiago-Alvarado, A.; Marquez-Garcia, J.; Gonzalez-Garcia, J., PDMS samples characterization with variations of synthesis parameters for tunable optics applications. *Heliyon* **2019,** *5* (12), e03064.
8. Rakotozandriny, K.; Bourg, S.; Papp, P.; Tóth, Á.; Horváth, D.; Lucas, I. T.; Babonneau, F.; Bonhomme, C.; Abou-Hassan, A., Investigating CaOx Crystal Formation in the Absence and Presence of Polyphenols under Microfluidic Conditions in Relation with Nephrolithiasis. *Crystal growth & design* **2020,** *20* (12), 7683-7693.
9. Kuliasha, C. A., Rodriguez, D., Lovett, A., Gower, L.B., In situ flow cell platform for examining calcium oxalate and calcium phosphate crystallization on films of basement membrane extract in the presence of urinary 'inhibitors'. *CrystEngComm* **2020,** *22* (8), 1448-1458.
10. Castiglione, V.; Sacre, P. Y.; Cavalier, E.; Hubert, P.; Gadisseur, R.; Ziemons, E., Raman chemical imaging, a new tool in kidney stone structure analysis: Case-study and comparison to Fourier Transform Infrared spectroscopy. *PloS one* **2018,** *13* (8), 1-18.
11. Edwards, H. G.; Seaward, M. R.; Attwood, S. J.; Little, S. J.; de Oliveira, L. F.; Tretiach, M., FT-Raman spectroscopy of lichens on dolomitic rocks: an assessment of metal oxalate formation. *The Analyst* **2003,** *128* (10), 1218-1221.
12. Cai, D., Neyer, A., Kuckuk, R., Heise, H.M., Raman, mid-infrared, near-infrared and ultraviolet–visible spectroscopy of PDMS silicone rubber for characterization of polymer optical waveguide materials. *Journal of Molecular Structure* **2010,** *976* (1-3), 274-281.
13. Çulha, M.; Lavrik, N.; Cullum, B. M.; Astilean, S., Surface-Enhanced Raman Scattering. **2012**.